The thermodynamic balance of the Weddell Gyre

Alberto C. Naveira Garabato[1*]
Jan D. Zika[1]
Loïc Jullion[2,3]
Peter J. Brown[4]
Paul R. Holland[5]
Michael P. Meredith[5]
Sheldon Bacon[4]

[1] University of Southampton, National Oceanography Centre, Southampton, SO14 3ZH, United Kingdom
[2] Aix-Marseille Université, CNRS / INSU, IRD, MIO, UM 110, 13288, Marseille, France
[3] Université de Toulon, CNRS / INSU, IRD, MIO, UM 110, La Garde, France
[4] National Oceanography Centre, Southampton, SO14 3ZH, United Kingdom
[5] British Antarctic Survey, Cambridge, CB3 0ET, United Kingdom

[*] Corresponding author: acng@noc.soton.ac.uk.

Abstract

The thermodynamic balance of the Weddell Gyre is assessed from an inverse estimate of the circulation across the gyre's rim. The gyre experiences a weak net buoyancy gain that arises from a leading-order cancellation between two opposing contributions, linked to two cells of water mass transformation and diapycnal overturning. The lower cell involves a cooling-driven densification of 8.4 ± 2.0 Sv of Circumpolar Deep Water and Antarctic Bottom Water near the gyre's southern and western margins. The upper cell entails a freshening-driven conversion of 4.9 ± 2.0 Sv of Circumpolar Deep Water into lighter upper-ocean waters within the gyre interior. The distinct role of salinity between the two cells stems from opposing salinity changes induced by sea ice production, meteoric sources and admixture of fresh upper-ocean waters in the lower cell, which contrasts with coherent reductions in salinity associated with sea ice melting and meteoric sources in the upper cell.

Key points

- The Weddell Gyre hosts two overturning cells with contrasting buoyancy forcings
- Lower cell involves cooling-driven densification of deep and bottom waters
- Upper cell entails freshening-driven lightening of deep water

1. Introduction

The subpolar Southern Ocean, lying to the south of the Antarctic Circumpolar Current (ACC), is a region of complex and vigorous interactions between the ocean, atmosphere and cryosphere. There, the heat transported by the ocean circulation across the ACC's southern boundary sustains seasonally intense sea-to-air heat fluxes and sea ice production [Holland and Kwok, 2012; Petty et al., 2014], and melts the floating edges of the Antarctic Ice Sheet [Rignot et al., 2013]. Significant changes in the salinity of surface waters are elicited by these ice – ocean interactions and the net precipitation that falls on the area. The weak upper-ocean stratification that characterises the region stems from a delicate balance between these multiple buoyancy sources and sinks [Martinson and Iannuzzi, 1998; Winton, 1999; Keeling and Visbeck, 2011]. The setting up of this balance is important because it regulates the rates at which mass and properties are exchanged between the ocean surface and the deep layers of the global ocean circulation [Rintoul and Naveira Garabato, 2013]. These exchanges exert a significant influence on the stability of the Antarctic Ice Sheet [Shepherd et al., 2012; Paolo et al., 2015], global sea level [Rye et al., 2014], the Earth's albedo [Brandt et al., 2005], the production of the dense Antarctic Bottom Water pervading much of the world ocean abyss (see Rintoul and Naveira Garabato [2013], and references therein), and the ocean – atmosphere partitioning of carbon [Watson and Naveira Garabato, 2006; Ferrari et al., 2014]. Circulating cyclonically between the Antarctic Peninsula and the southwestern Indian Ocean, the Weddell Gyre spans over one quarter of the subpolar Southern Ocean, and has long been singled out as a major region of water mass transformations and diapycnal overturning (see Orsi et al. [1993] and Jullion et al. [2014], and references therein). The gyre is forced by westerly and easterly winds over its northern and southern edges, respectively, favouring upwelling in the gyre's centre and downwelling along its southern limb. Concurrent to this mechanical forcing, the gyre is also subject to strong and complex thermodynamic drivers.

This is manifested most conspicuously in the significant cooling and freshening undergone by waters circulating within the gyre [Jullion et al., 2014], in the pronounced seasonal cycle of sea ice advance and retreat over the gyre [Zwally et al., 2002], and in the formation of super-cooled waters in ice shelf cavities along the gyre's ice-bounded poleward rim [Nicholls et al., 2009].

In this article, we quantitatively assess the thermodynamic balance of the Weddell Gyre. Specifically, we elucidate the relative roles of air-ice-ocean heat exchanges, sea ice production and melting, and meteoric freshwater sources in forcing water mass transformations and diapycnal overturning within the gyre. An introduction to our data set and methodology is provided in section 2. The key features of the gyre's circulation identified in preceding analyses of that data set are also outlined there. Section 3 presents our diagnosis of the thermodynamic balance of the gyre. Finally, our main findings are reviewed and their implications discussed in section 4.

2. Data, regional circulation, and methods

2.1. Data

The central data set of this analysis consists of three oceanographic transects encompassing the Weddell Gyre (Fig. 1a) that were conducted within a 2-year period (2008 – 2010): the I6S section, a quasi-meridional line along 30°E between South Africa and Antarctica occupied in February – March 2008; and the eastern and western (east and west of 19°W, respectively) segments of the ANDREX section, a quasi-zonal line between 30°E and the tip of the Antarctic Peninsula, occupied in January 2009 and March – April 2010, respectively. The set of variables measured along these transects included hydrographic properties (temperature, salinity and pressure; Fig. 1b), horizontal velocity, and the freshwater tracer $\delta^{18}O$. An

extensive account of these oceanographic sections and data sets is provided by Jullion et al. [2014] and Brown et al. [2014].

2.2. Regional circulation

An optimal, self-consistent estimate of the circulation and physical exchanges across the rim of the Weddell Gyre was obtained by Jullion et al. [2014], using a box inverse model of the region bounded by the I6S and ANDREX transects and a hydrographic section across the southwestern Weddell Sea, and including mobile sea ice and eddy fluxes (see Supporting Information for a description of the inverse model). This estimate is representative of the annual-mean state of the gyre in 2008 – 2010 within uncertainties, as the bias introduced by the summertime focus of the hydrographic observations was assessed with the eddy-permitting Southern Ocean State Estimate [Mazloff et al., 2010] and factored into the prior uncertainties of all equations and unknowns in the inverse model [Jullion et al., 2014]. An overview of the main features of the circulation across the gyre's boundary is given by Figure 1b. There is a net equatorward freshwater (approximately equivalent to volume) transport through the combined ANDREX – I6S transect of 51 ± 23 mSv, which is balanced by precipitation within and ablation at the ice-bound edges of the gyre. The majority of this transport (38 ± 23 mSv) occurs in liquid form, and the rest (13 ± 1 mSv) as sea ice. (Note that the inversion-derived rates of meteoric freshwater input to and sea ice export from the Weddell Gyre are consistent with quasi-independent estimates of those rates from an analysis of the $\delta^{18}O$ measurements along the ANDREX – I6S section within uncertainties [Brown et al., 2014].) Heat enters the Weddell Gyre across the combined section at a rate of 36 ± 13 TW, where the bulk of the heat flux (26 ± 13 TW) is effected by the mean ocean circulation (strictly, the circulation explicitly resolved by the sections), and the rest by transient eddies (5

± 1 TW) and sea ice (5 ± 1 TW). This is balanced by oceanic heat loss to the atmosphere and ice shelves overlying the gyre.

The horizontal circulation through the combined ANDREX – I6S transect exhibits two major features (Fig. 1b): a 68 ± 18 Sv anticyclonic recirculation of the southern edge of the ACC through the northeastern corner of the transect, which has minimal influence on the gyre's physical budgets [Jullion et al., 2014]; and a Weddell Gyre transport of 54 ± 15 Sv. The latter entails a substantial throughflow component, by which 13 ± 4 Sv enters the gyre's eastern rim from the Indian sector and is exported northward across the ANDREX section.

The vertical (overturning) circulation in the Weddell Gyre has an asymmetric double-celled structure (Fig. 1c): 13.3 ± 3.2 Sv of Circumpolar Deep Water (CDW) and Antarctic Bottom Water (AABW) lighter than $\gamma = 28.345 ± 0.008$ kg m^{-3} (where γ is the neutral density variable of Jackett and MacDougall [1997]) are transformed into both denser AABW by downslope convection around the gyre's southwestern rim (8.4 ± 2.0 Sv), and upper-ocean waters lighter than $\gamma = 28.061 ± 0.011$ kg m^{-3} by mid-gyre upwelling (4.9 ± 2.0 Sv). The inter-cell boundary is defined by the $\gamma = 28.154 ± 0.007$ kg m^{-3} surface, which is the densest isopycnal for which the volume transport integrated over denser classes matches the δ^{18}O-derived meteoric freshwater transport in those classes. This is equivalent to the common definition of an overturning cell boundary as the zero-crossing of the overturning streamfunction (e.g., Mazloff et al. [2010]), but accounts for the net meteoric freshwater input to the gyre.

2.3. Methods

Our investigation of the thermodynamic balance of the Weddell Gyre is founded on the calculation of residual volume transports in a set of 2-d spaces, each of which is defined by a pair of scalar properties of the flow across the combined ANDREX – I6S section. The residual volume transport T_{AB} in a space defined by the scalar pair (A,B) is given by

$$T_{AB}(A_i, B_j) = \iint \delta(A_i, B_j)\, v_\perp(l,z)\, dl\, dz \;, \qquad\qquad (1)$$

where $v_\perp(l,z)$ is the horizontal velocity perpendicular to the section; l is distance along the section; z is height; and $\delta(A_i, B_j)$ is a delta function that equals 1 for $(A,B) = (A_i, B_j)$ and is 0 otherwise[1]. Using this transport variable, the residual-transport-weighted-mean value of a scalar C may be computed as

$$\overline{C_{AB}} = \left. \iint C(A,B)\, T_{AB}(A,B)\, dA\, dB \middle/ \iint T_{AB}(A,B)\, dA\, dB \right. \qquad (2)$$

This expression may be evaluated for any arbitrary subset of (A,B) space [for example, that corresponding to flow into the gyre $(T_{AB} < 0)$, to flow out of the gyre $(T_{AB} > 0)$, or to subsets of these associated with water in a given density class], and provides a useful metric of the characteristic value of C for water flowing in that space. Note that only liquid seawater (i.e. not sea ice) is considered in (1) - (2). As we do not know the distribution of isopycnal eddy fluxes (of volume or a scalar property) in $A - B$ space, we assume those fluxes to be distributed identically in that space to the mean transports on each isopycnal surface. This assumption is not critical to our results, as eddy fluxes are comparatively minor contributors to the volume, heat and freshwater fluxes across the gyre boundary [Jullion et al., 2014].

To aid in the interpretation of the gyre's thermodynamical balance, it is useful to decompose the change in γ between the inflows to and outflows from the gyre (denoted $\Delta\gamma = \overline{\gamma^{out}}_{\theta S}$ - $\overline{\gamma^{in}}_{\theta S}$, where superscripts *out* and *in* respectively refer to outflows and inflows) into approximate contributions from changes in potential temperature (θ) and in salinity (S). The decomposition is effected by approximating the area of $\gamma(\theta, S)$ space bounded by $(\overline{\theta^{out}}_{\theta S} \leq \theta \leq \overline{\theta^{in}}_{\theta S}, \overline{S^{out}}_{\theta S} \leq S \leq \overline{S^{in}}_{\theta S})$ by a plane surface, and computing $\partial\gamma/\partial\theta$ and $\partial\gamma/\partial S$ as the

---

[1] Note that, in implementing this calculation numerically, A and B are defined on a regular grid and treated as piecewise-constant over each grid cell [i,j].

plane's slopes in the directions of the θ and S axes. These contributions are respectively defined as $\Delta\gamma_\theta = (\partial\gamma/\partial\theta)\ \Delta\theta$ and $\Delta\gamma_S = (\partial\gamma/\partial S)\ \Delta S$, where $\Delta\theta = \overline{\theta^{out}}_{\theta S} - \overline{\theta^{in}}_{\theta S}$ and $\Delta S = \overline{S^{out}}_{\theta S} - \overline{S^{in}}_{\theta S}$. As the dependence of γ on θ and S is nonlinear, the residual-transport-weighted-mean θ - S coordinates of the inflow (or outflow) lie on a γ surface that is modestly different from $\overline{\gamma^{in}}_{\theta S}$ (or $\overline{\gamma^{out}}_{\theta S}$), and the decomposition is only approximate, i.e. $\Delta\gamma \neq \Delta\gamma_\theta + \Delta\gamma_S$. The change in the buoyancy content of (any volume-conserving portion of) the gyre associated with $\Delta\gamma$ is computed as $b = -g\ \rho_0^{-1}\Delta\gamma \iint T_{\theta S}\ d\theta\ dS\ /\ \iint d\theta\ dS$, where g is the acceleration due to gravity, ρ_0 is a reference density, and the integral is taken for either the inflows or the outflows and over the area of $\theta - S$ space entering the calculation of $\Delta\gamma$.

Changes in S (i.e. ΔS) between the inflows to and outflows from the gyre are decomposed into the four components in the δ^{18}O-based freshwater source analysis of Brown et al. [2014], as

$$\Delta S = \Delta S_{SIM} + \Delta S_{MET} + \Delta S_{WW} + \Delta S_{CDW} = (S_{SIM} - \overline{S^{in}}_{\theta S})\ \Delta f_{SIM} + (S_{MET} - \overline{S^{in}}_{\theta S})\ \Delta f_{MET} + (S_{WW} - \overline{S^{in}}_{\theta S})\ \Delta f_{WW} + (S_{CDW} - \overline{S^{in}}_{\theta S})\ \Delta f_{CDW}. \tag{3}$$

Here, f_{SIM}, f_{MET}, f_{WW} and f_{CDW} sum up to 1, and respectively refer to freshwater fractions associated with sea ice melt, meteoric freshwater and the 'purest' Winter Water (WW) and CDW entering the gyre across the I6S transect. These components are characterised by salinities of $S_{SIM} = 5$, $S_{MET} = 0$, $S_{WW} = 34.246$ and $S_{CDW} = 34.752$. Note that the WW entering the Weddell Gyre from the east acquires its low salinity from the accumulation of meteoric inputs outside the gyre. See Brown et al. (2014) for a discussion of the rationale of these end-member choices and their analysis methodology. The Δ operators on the right hand side of (3) are equivalent to those defined above for γ, θ and S. The change in γ associated with each of the four components of ΔS in (3) is estimated following the same approach as for $\Delta\gamma_S$.

As discussed by Brown et al. [2014], the estimates of freshwater fractions in surface waters are likely to suffer from significant sampling-related biases. The ANDREX – I6S δ^{18}O data set was collected in three different months and years, thereby aliasing the pronounced seasonal variability in sea ice production that affects the gyre's upper-ocean layers. Following Brown et al. (2014), we surmise that the seasonal bias in δ^{18}O-derived meteoric freshwater fraction is negligible, as the δ^{18}O- and inversion-derived estimates of the meteoric freshwater input to the Weddell Gyre agree within uncertainties (section 3); and argue that δ^{18}O-derived sea ice melt fractions in the CDW and AABW layers are representative of annual-mean values, as the age of those water masses at the gyre's rim generally exceeds one year [Huhn et al., 2013]. In order to estimate the seasonal bias in δ^{18}O-derived sea ice melt transports in the gyre's upper-ocean layers, we adjust the δ^{18}O field in the surface waters and WW to values measured in a mid-winter cruise in the central Weddell Sea, and re-calculate the transports (see Brown et al. [2014] for details of this bias estimation procedure).

Uncertainties in all transports and derived variables are estimated using a Monte Carlo approach (outlined in the Supporting Information) and expressed as one-standard-deviation error bars. The exception is the annual-mean sea ice melt rates estimated from wintertime δ^{18}O measurements, the expected uncertainty of which is roughly a factor of 2 [Brown et al., 2014] and not quoted explicitly.

3. Results

An overview of the thermodynamic balance of the Weddell Gyre is provided by Figure 2d, which displays $T_{\theta S}$, the rate at which water leaves the gyre across the combined ANDREX – I6S section as a function of $\theta - S$ class. The residual-transport-weighted-mean θ, S and γ of the water entering and leaving the gyre are indicated in the figure and listed in Table 1. Figures 2a and 2g respectively show the integrals of $T_{\theta S}$ for all θ classes and for all S classes.

Circulation around the gyre entails a net cooling ($\Delta\theta$ = -0.066 ± 0.004°C) and freshening (ΔS = -0.013 ± 0.005), as expected from the oceanic heat loss and meteoric freshwater input that occurs in the region (section 2). These thermohaline changes are approximately density-compensating ($\Delta\gamma_\theta$ = 0.010 ± 0.001 kg m^{-3}; $\Delta\gamma_S$ = -0.010 ± 0.003 kg m^{-3}; $\Delta\gamma$ = (-3 ± 2) × 10^{-4} kg m^{-3}), and are associated with a modest oceanic buoyancy gain of 238 ± 172 m^4 s^{-3}. We will next show that this weak net buoyancy forcing arises from a leading-order cancellation between two opposing contributions, which underpins the diapycnal bifurcation of mid-depth waters in the gyre and associated double-celled overturning structure.

To elicit this point, we consider how the major water mass transformations outlined in section 2 are manifested in Figures 2a, 2d and 2g. There is a preferential consumption of comparatively warm and saline CDW and AABW in the 28.061 < γ < 28.345 kg m^{-3} class, and a net production of denser AABW and lighter upper-ocean waters that is respectively associated with the lower and upper cells of the regional overturning. While both of the produced water types are cooler and fresher than the consumed waters, temperature (salinity) exerts a dominant control on buoyancy for the lower (upper) cell. The oceanic buoyancy loss implicated in the lower cell (10332 ± 3652 m^4 s^{-3}) and the buoyancy gain associated with the upper cell (10570 ± 1329 m^4 s^{-3}) are individually two orders of magnitude larger than the net buoyancy gain in the gyre.

To gain insight into how the leading-order cancellation in the gyre's buoyancy budget comes about, it is instructive to examine in detail the thermodynamic balance of each individual overturning cell. The net cooling ($\Delta\theta$ = -0.149 ± 0.002°C) and freshening (ΔS = -0.004 ± 0.002) implicated in the lower cell are respectively more and less pronounced than those associated with the gyre as a whole (Figures 2a and 2g). The emphasis of cooling ($\Delta\gamma_\theta$ = 0.032 ± 0.004 kg m^{-3}) relative to freshening ($\Delta\gamma_S$ = -0.015 ± 0.008 kg m^{-3}) in the lower cell results in a substantial net densification ($\Delta\gamma$ = 0.028 ± 0.008 kg m^{-3}). In contrast, the net

cooling ($\Delta\theta$ = -0.011 ± 0.003°C) and freshening (ΔS = -0.018 ± 0.004) implicated in the upper cell are respectively less and more pronounced than those associated with the gyre as a whole (Figures 2a and 2g). The emphasis of freshening ($\Delta\gamma_S$ = -0.020 ± 0.005 kg m^{-3}) relative to cooling ($\Delta\gamma_\theta$ = 0.003 ± 0.001 kg m^{-3}) in the upper cell results in a substantial net lightening ($\Delta\gamma$ = -0.019 ± 0.004 kg m^{-3}). This set of transformations is synthesised in Table 1.

The cooling associated with both overturning cells is understood to arise from the loss of heat from upper-ocean waters circulating in the Weddell Gyre to the generally colder overlying atmosphere and ice shelves. In contrast, the freshening implicit in both cells has a less obvious interpretation, as it convolves contributions from precipitation and evaporation, ice-shelf melting and freezing, and sea ice production and melting. The freshwater component of the gyre's thermodynamic balance may be unravelled by considering how each of the freshwater components changes between the inflows to and the outflows from the region. To this end, Figures 2e and 2f respectively display $T_{\theta f SIM}$ and $T_{\theta f MET}$, the rates at which water leaves the gyre across the combined ANDREX – I6S section as a function of $\theta - f_{SIM}$ and $\theta - f_{MET}$ classes. Figures 2b and 2c show the integrals of $T_{\theta f SIM}$ and $T_{\theta f MET}$ for the entire range of θ. Results of this freshwater source analysis are synthesised in Table 1.

The overall freshening of the gyre is, as expected, induced by a source of meteoric freshwater (Δf_{MET} = 0.05 ± 0.02%; ΔS_{MET} = -0.017 ± 0.007; Figures 2c and 2f) of 45 ± 13 mSv, which agrees with the inversion-derived export of liquid freshwater from the region (38 ± 23 mSv; section 2.2). The freshening is tempered by a net production of sea ice in the gyre (Δf_{SIM} = -0.06 ± 0.02%; Figures 2b and 2e) and an unphysical transfer between the CDW and WW end-members (Δf_{CDW} = -2.84 ± 0.62%; Δf_{WW} = 2.85 ± 0.64%; Table 1). As the diagnosed Δf_{MET} is representative of the annual-mean state of the gyre (section 2.3), the net salinification associated with Δf_{SIM}, Δf_{CDW} and Δf_{WW} may be interpreted as an annual-mean estimate of

ΔS_{SIM} of 0.004 ± 0.002, because the similarity in the $\delta^{18}O$ values of the latter three end-members would lead to seasonal variations in Δf_{SIM} being compensated by the imbalance between Δf_{CDW} and Δf_{WW}. As discussed by Brown et al. [2014], the rate of sea ice production and export derived from the summertime $\delta^{18}O$ data (51 ± 11 mSv) accounts for the entire meteoric freshwater input to the region. This is inconsistent with the gyre's observed freshening, and stems from the seasonal sampling bias in upper-ocean waters. Those authors use wintertime $\delta^{18}O$ measurements to estimate an annual-mean rate of sea ice production of 15 − 20 mSv (corresponding to $\Delta f_{SIM} \sim$ -0.015% and $\Delta S_{SIM} \sim$ 0.004), which is in line with the inversion-derived rate of sea ice export from the gyre (13 ± 1 mSv; section 2.2) and the annual-mean estimate of ΔS_{SIM} above. We conclude that approximately one quarter of the gyre's freshening induced by the input of meteoric freshwater by precipitation and ablation is offset by sea ice production and export from the region (i.e. ΔS = -0.013 ± 0.005; ΔS_{MET} = -0.017 ± 0.007; ΔS_{SIM} = 0.004 ± 0.002). This result carries over to the relative significance of meteoric freshwater sources and sea ice production in determining $\Delta \gamma_S$.

Partitioning the gyre's freshwater balance into the contributions of the two overturning cells reveals the meteoric and sea ice freshwater components to play distinct roles in each cell. The freshening induced by the addition of meteoric freshwater to waters in the lower cell (Δf_{MET} = 0.10 ± 0.01%; ΔS_{MET} = -0.035 ± 0.004; Figures 2c and 2f) is overwhelmed by the salinification of those waters associated with sea ice production (Δf_{SIM} = -0.25 ± 0.01%; ΔS_{SIM} = 0.074 ± 0.004; Figures 2b and 2e). The net freshening implicit in the lower cell is primarily related to the admixture of WW (Δf_{WW} = 8.77 ± 0.31%; ΔS_{WW} = -0.037 ± 0.002) from and loss of CDW (Δf_{CDW} = -8.62 ± 0.27%; ΔS_{CDW} = -0.006 ± 0.002) to the upper cell (Table 1). In contrast, the freshening of waters in the upper cell is associated with the combined action of sea ice melt (Δf_{SIM} = 0.05 ± 0.02%; ΔS_{SIM} = -0.016 ± 0.006; Figures 2b and 2e) and meteoric

freshwater sources ($\Delta f_{MET} = 0.02 \pm 0.02\%$; $\Delta S_{MET} = $ -0.007 $\pm$ 0.006; Figures 2c and 2f), moderated by a loss of WW ($\Delta f_{WW} = $ -0.96 $\pm$ 0.53%; $\Delta S_{WW} = 0.002 \pm 0.001$) to and gain of CDW ($\Delta f_{CDW} = 0.89 \pm 0.51\%$; $\Delta S_{CDW} = 0.002 \pm 0.001$) from the lower cell (Table 1). The contribution of sea ice melt to the freshening of waters in the upper cell diagnosed here from summertime measurements is likely to be an overestimate of the annual-mean value. Assessing the seasonal bias from wintertime $\delta^{18}O$ measurements as in Brown et al. [2014] (section 2.3), the annual-mean rate of upper-cell freshening by sea ice melt may be estimated to be roughly half of the summer value ($\Delta f_{SIM} \sim 0.02\%$ and $\Delta S_{SIM} \sim 0.006$). Given the crudeness of this assessment, the summer rate is quoted henceforth.

The diagnosed pattern of freshwater flow within the Weddell Gyre suggests that net sea ice production in the region is focussed on the continental shelves of the southwestern and western Weddell Sea, where the density classes of the lower cell outcrop [e.g., Nicholls et al., 2009], and that sea ice melting primarily affects regions of the gyre further offshore, where the range of densities of upper-ocean waters is characteristic of the upper cell [Jullion et al., 2014]. Meteoric freshwater sources act to freshen the entire surface of the gyre. The net transfer of WW from the upper cell to the lower cell is consistent with the occurrence of entrainment processes at the continental shelf break, where plumes of recently formed dense shelf waters descend downslope [Nicholls et al., 2009; Jullion et al., 2014]; and the net transfer of CDW from the lower cell to the upper cell is consistent with mid-gyre upwelling [Jullion et al., 2014]. Thus, the insignificance of salinity in the densification of waters in the lower cell stems from the leading-order cancellation between salinity changes associated with sea ice production, meteoric freshwater input and WW admixture in the shelf-slope areas of the southern and western Weddell Sea. Conversely, the importance of salinity in the lightening of waters in the upper cell relates to the mutual reinforcement of salinity

reductions induced by sea ice melting and meteoric freshwater input, modestly offset by the admixture of CDW from the lower cell.

4. Conclusions

The thermodynamic balance of the Weddell Gyre is synthesised schematically in Figure 3. Waters circulating within the gyre experience a net cooling and freshening that are almost perfectly density-compensating. The net cooling entails the loss of 36 ± 13 TW of heat to the overlying atmosphere and Antarctic Ice Sheet, of which 5 ± 1 TW are expended in the production and export of $13 - 20$ mSv of sea ice. In turn, the net freshening stems from the input of 51 ± 23 mSv of meteoric freshwater by precipitation and ablation, with approximately one quarter of the meteoric-induced freshening being offset by the formation and export of sea ice.

The weak net buoyancy forcing of the Weddell Gyre stems from a leading-order cancellation between two opposing contributions, associated with two distinct cells of water mass transformation and diapycnal overturning. In the lower cell, CDW and AABW in the 28.154 $< \gamma < 28.345$ kg m^{-3} class are made denser at a rate of 8.4 ± 2.0 Sv, primarily as a consequence of the loss of 33 ± 13 TW of oceanic heat along the gyre's southern and western margins. The cooling-related densification is tempered by a modest freshening, which results from the competing effects of meteoric inputs (38 ± 23 mSv) and admixture of fresh WW, and salinification associated with the production of 94 ± 20 mSv of sea ice — the major fraction of which melts offshore of the continental shelves. Without this salinification, the buoyancy gain induced by meteoric- and WW-related freshening would overwhelm the buoyancy loss due to cooling (Table 1). Thus, sea ice formation plays a catalytic role in enabling the densification that is intrinsic to the lower cell. It is also notable that an O(10%) variation to any individual freshwater source / sink term can change the sign of the lower

cell's buoyancy budget (Table 1), suggesting that this cell may be particularly sensitive to climatic perturbations in freshwater forcing. In the upper cell, CDW in the $28.061 < \gamma < 28.154$ kg m^{-3} class upwells into lighter, upper-ocean layers at a rate of 4.9 ± 2.0 Sv, primarily as a result of freshening by sea ice melting and meteoric sources. This lightening is moderated only weakly by cooling, linked to an oceanic heat loss of 3 ± 1 TW.

Note that, since our characterisation of the thermodynamic balance of the Weddell Gyre integrates the effects of highly seasonal processes (e.g., oceanic heat loss and the cycle of sea ice production and melting) over an annual cycle, it is likely to conceal prominent seasonality in the thermodynamic forcing of the circulation. The oceanic heat loss and sea ice production that underpin the lower cell are expected to peak in winter, whereas the sea ice melting that is integral to the upper cell is most intense in summer [Petty et al., 2014]. This suggests that the densification (lightening) of water masses associated with the lower (upper) cell is likely to be focussed in winter (summer).

Our assessment of the thermodynamic forcing of water mass transformations and diapycnal overturning within the Weddell Gyre stresses the significance of the region in hosting a diapycnal bifurcation of mid-depth Southern Ocean waters, rather than solely densification and downwelling as commonly highlighted in the literature. The occurrence of this double-celled overturning is founded on two key thermodynamic drivers: oceanic heat loss, which underpins downwelling at the gyre's poleward rim; and the seasonal cycle of sea ice production and melting, which both offsets the lightening action of meteoric freshwater sources in downwelling areas and enables upwelling in the gyre interior. To date, discussions of the consequences for ocean circulation of past and future climatic changes in these drivers have generally focussed on the formation and sinking of AABW [e.g., Ferrari et al., 2014; de Lavergne et al., 2014]. Our results suggest that upwelling in the subpolar Southern Ocean is likely to be affected by such changes too, and thus deserves greater attention.

References

Brandt, R. E., S. G. Warren, A. P. Worby, and T. C. Grenfell (2005), Surface albedo of the Antarctic sea ice zone, *J. Clim., 18*, doi:10.1175/JCLI3489.1.

Brown, P. J., M. P. Meredith, L. Jullion, A. Naveira Garabato, S. Torres-Valdés, P. Holland, M. J. Leng, and H. Venables (2014), Freshwater fluxes in the Weddell Gyre: Results from δ^{18}O, *Phil. Trans. Roy. Soc. A, 372*, doi: 10.1098/rsta.2013.0298.

de Lavergne, C., J. B. Palter, E. D. Galbraith, R. Bernardello, and I. Marinov (2014), Cessation of deep convection in the open Southern Ocean under anthropogenic climate change, *Nature Clim. Change, 4*, 278-282.

Ferrari, R., M. F. Jansen, J. F. Adkins, A. Burke, A. L. Stewart, and A. F. Thompson (2014), Antarctic sea ice control on ocean circulation in present and glacial climates, *Proc. Nat. Acad. Sci., 111*, 8753-8758.

Holland, P. R., and R. Kwok (2012), Wind-driven trends in Antarctic sea-ice drift, *Nature Geosci., 5*, 872-875.

Huhn, O., M. Rhein, M. Hoppema, and S. van Heuven (2013), Decline of deep and bottom water ventilation and slowing down of anthropogenic carbon storage in the Weddell Sea, 1984–2011, *Deep-Sea Res. I*, 76, 66-84.

Jullion, L., A. C. Naveira Garabato, S. Bacon, M. P. Meredith, P. J. Brown, S. Torres-Valdés, K. G. Speer, P. R. Holland, J. Dong, D. Bakker, M. Hoppema, B. Loose, H. J. Venables, W. J. Jenkins, M.-J. Messias, and E. Fahrbach (2014), The contribution of the Weddell Gyre to the lower limb of the global overturning circulation, *J. Geophys. Res., 119*, 3357-3377.

Keeling, R. F., and M. Visbeck (2011), On the linkage between Antarctic surface water stratification and global deep-water temperature, *J. Clim., 24*, 3545-3557.

Martinson, D. G., and R. A. Iannuzzi (1998), Antarctic ocean-ice interaction: Implications from ocean bulk property distributions in the Weddell Gyre, in M. Jeffries (ed.), *Antarctic Research Series, Antarctic Sea Ice: Physical Processes, Interactions and Variability*, American Geophysical Union, Boston, pp. 243-271.

Mazloff, M. R., P. Heimbach, and C. Wunsch (2010), An eddy-permitting Southern Ocean State Estimate, *J. Phys. Oceanogr., 40*, 880-899.

Nicholls, K. W., S. Østerhus, K. Makinson, T. Gammelsrød, and E. Fahrbach (2009), Ice-ocean processes over the continental shelf of the southern Weddell Sea, Antarctica: A review, *Rev. Geophys., 47*, doi: 10.1029/2007RG000250.

Orsi, A. H., W. D. Nowlin, and T. Whitworth (1993), On the circulation and stratification of the Weddell Gyre, *Deep-Sea Res. I, 40*, 169-203.

Paolo, F. S., H. A. Fricker, and L. Padman (2015), Volume loss from Antarctic ice shelves is accelerating, *Science, 348*, 327-331.

Petty, A. A., P. R. Holland, and D. L. Feltham (2014), Sea ice and the ocean mixed layer over the Antarctic shelf seas, *Cryosph., 8*, 761-783.

Rignot, E., S. Jacobs, J. Mouginot, and B. Scheuchl (2013), Ice-shelf melting around Antarctica, *Science, 341*, 266-270.

Rintoul, S. R., and A. C. Naveira Garabato (2013), Dynamics of the Southern Ocean circulation, in, G. Siedler, S. Griffies, J. Gould, and J. Church (eds.), *Ocean Circulation and Climate: A 21st Century Perspective,* Academic Press, Oxford, pp. 471-492.

Rye, C. D., A. C. Naveira Garabato, P. R. Holland, M. P. Meredith, A. J. G. Nurser, C. W. Hughes, A. C. Coward, and D. J. Webb (2014), Rapid sea-level rise along the Antarctic margins in response to increased glacial discharge, *Nature Geosci., 7*, 732-735.

Shepherd, A., and 46 others (2012), A reconciled estimate of ice-sheet mass balance, *Science, 338*, 1183-1189.

Watson, A. J.. and A. C. Naveira Garabato (2006), The role of Southern Ocean mixing and upwelling in glacial-interglacial atmospheric CO_2 change, *Tellus, 58B*, 73-87.

Winton, M. (1999), Polar water column stability, *J. Phys. Oceanogr., 29*, 1368-1371.

Zwally, H. J., J. C. Comiso, C. L. Parkinson, D. J. Cavalieri, and P. Gloersen (2002), Variability in Antarctic sea ice 1979-1998, *J. Geophys. Res., 107*, doi: 10.1029/2000JC000733.

Table 1. Integrated residual volume transports and residual-transport-weighted-mean θ, S, f_{SIM}, f_{MET}, f_{WW}, f_{CDW} and γ across the combined ANDREX – I6S section for the inflow, outflow and their difference. The three lines of values in each grid cell correspond (from top to bottom) to the total Weddell Gyre flow, the upper cell, and the lower cell. In the 'difference' row, $\overline{S_{\theta S}}$ column, the three values in brackets denote (in this order) the changes in $\overline{S_{\theta S}}$ induced by sea ice melt, meteoric freshwater input, and variations in the WW and CDW fractions. In the 'difference' row, $\overline{\gamma_{\theta S}}$ column, the two values in brackets indicate the estimated changes in $\overline{\gamma_{\theta S}}$ induced by variations in θ and S. See section 2.3 for a description of the methodology.

	$\iint T_{\theta S}\, d\theta\, dS / \iint d\theta\, dS$ / 10^3 m³ s⁻¹	$\overline{\theta_{\theta S}}$ / °C	$\overline{S_{\theta S}}$	$\overline{fSIM_{\theta S}}$ / %	$\overline{fMET_{\theta S}}$ / %	$\overline{fWW_{\theta S}}$ / %	$\overline{fCDW_{\theta S}}$ / %	$\overline{\gamma_{\theta S}}$ / kg m⁻³
Inflow	(-96.1 ± 6.4) × 10³	0.311 ± 0.007	34.553 ± 0.006	-0.61 ± 0.16	0.55 ± 0.17	43.04 ± 1.06	57.09 ± 1.02	28.055 ± 0.012
	(-58.4 ± 3.9) × 10³	0.478 ± 0.006	34.480 ± 0.005	-0.46 ± 0.12	0.66 ± 0.13	46.65 ± 0.87	53.27 ± 0.81	27.929 ± 0.007
	(-37.7 ± 2.7) × 10³	0.050 ± 0.004	34.666 ± 0.003	-0.85 ± 0.09	0.41 ± 0.09	37.43 ± 0.56	63.01 ± 0.61	28.251 ± 0.010
Outflow	(96.1 ± 6.4) × 10³	0.245 ± 0.008	34.540 ± 0.006	-0.67 ± 0.17	0.60 ± 0.18	45.89 ± 1.07	54.25 ± 1.03	28.055 ± 0.012
	(58.4 ± 3.9) × 10³	0.467 ± 0.007	34.462 ± 0.005	-0.39 ± 0.13	0.68 ± 0.13	45.69 ± 0.89	54.16 ± 0.84	27.910 ± 0.008
	(37.7 ± 2.7) × 10³	-0.099 ± 0.004	34.662 ± 0.003	-1.10 ± 0.09	0.51 ± 0.10	46.20 ± 0.58	54.39 ± 0.60	28.280 ± 0.011
Difference (Outflow – Inflow)	36 ± 5	-0.066 ± 0.004	-0.013 ± 0.005 [0.018, -0.017, -0.014]	-0.06 ± 0.02	0.05 ± 0.02	2.85 ± 0.64	-2.84 ± 0.62	(-3 ± 2) × 10⁻⁴ [0.010, -0.010]
	0 ± 9	-0.011 ± 0.003	-0.018 ± 0.004 [-0.016, -0.007,	0.07 ± 0.02	0.02 ± 0.02	-0.96 ± 0.53	0.89 ± 0.51	-0.019 ± 0.004 [0.003, -

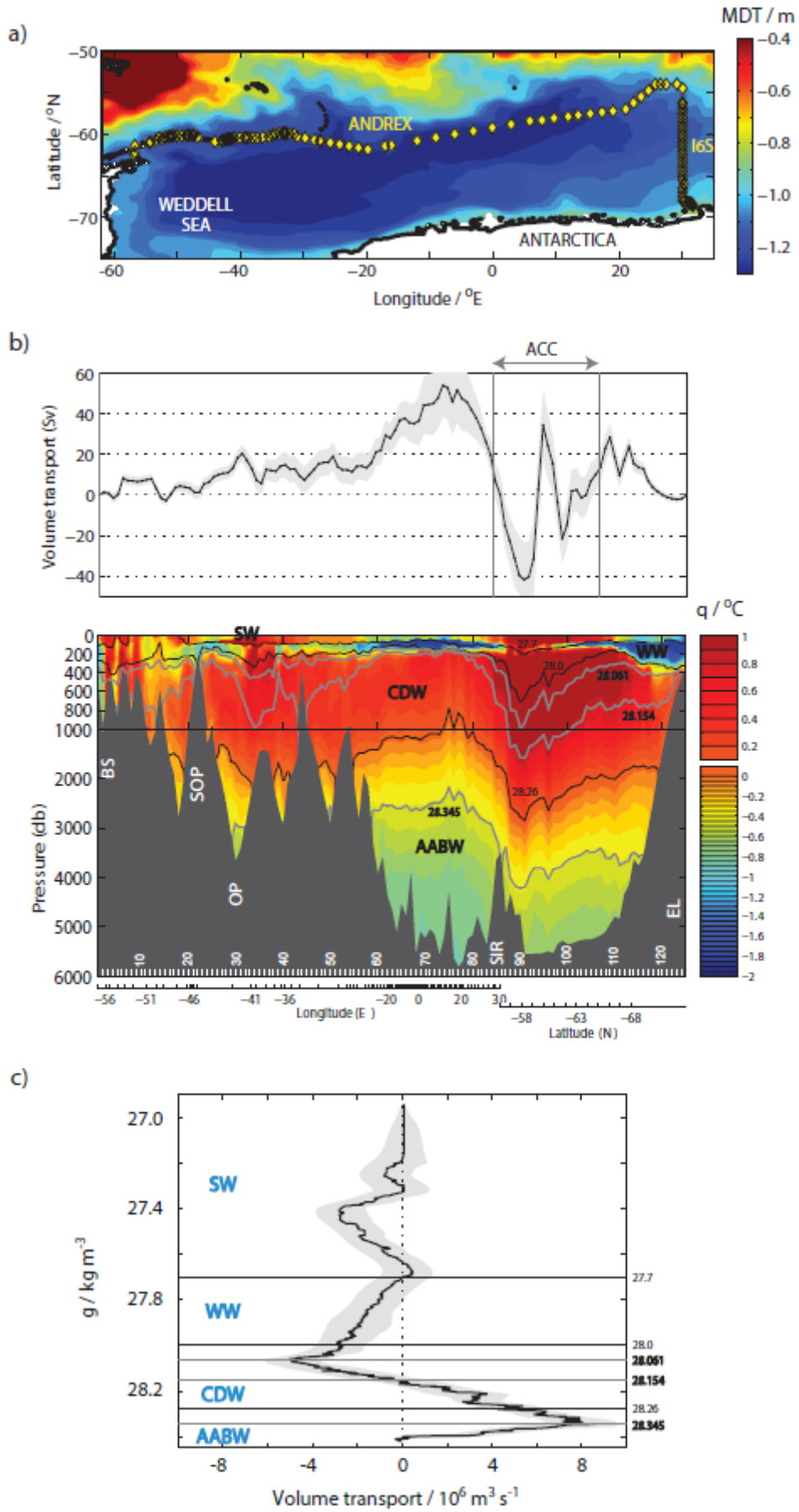|			0.005]					0.020]
	36 ± 5	-0.149 ± 0.002	-0.004 ± 0.002 [0.074, -0.035, -0.043]	-0.25 ± 0.01	0.10 ± 0.01	8.77 ± 0.31	-8.62 ± 0.27	0.028 ± 0.008 [0.032, -0.015]

a)

b)

c)

Figure 1. Overview of the setting and results of the Weddell Gyre inverse model of Jullion et al. [2014]. (a) Map of the ANDREX and I6S stations (diamonds). The (2005-2010 time-averaged) mean dynamic topography (MDT) in the Southern Ocean State Estimate (Mazloff et al., 2010) is shown by the background shading. (b) Upper panel: full-depth volume transport across the combined ANDREX – I6S section (positive transport directed out of the gyre). The uncertainty is indicated in grey, and the segment of the section within the ACC is marked on the upper axis. Lower panel: vertical section of potential temperature (colour) and selected neutral density surfaces (contours), with station number (labelled in white) as the horizontal axis. Isopycnals separating major water masses (SW = surface waters; WW = Winter Water; CDW = Circumpolar Deep Water; AABW = Antarctic Bottom Water) are indicated by black contours and labels, and those marking the transport maxima of and the boundary between the gyre's two overturning cells are shown by grey contours and labels. The following topographic features are indicated: Bransfield Strait (BS), EL (Enderby Land), OP (Orkney Passage), SOP (South Orkney Plateau). (c) Accumulated volume transport across the combined ANDREX – I6S section, with water masses and isopycnals indicated as in (b). The uncertainty is shown in grey.
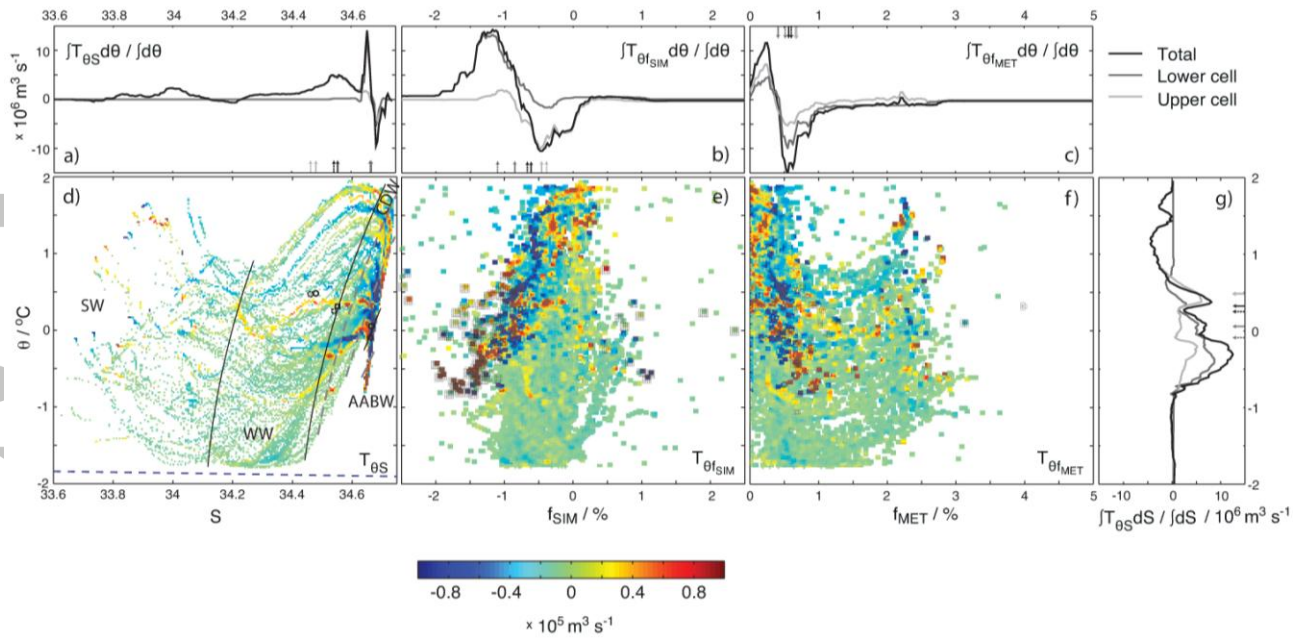
Figure 2. Overview of residual volume transports across the combined ANDREX – I6S section. (a) Residual volume transports as a function of S class. Black, dark grey and light grey lines respectively refer to the total, lower-cell and upper-cell flows. The small arrows at the base of the panel indicate residual-transport-weighted-mean S values, with the same colour coding as the lines. Solid and dashed arrows are associated with inflows and outflows, respectively. (b) Residual volume transports as a function of f_{SIM} class. Lines and arrows follow the convention in (a). (c) Residual volume transports as a function of f_{MET} class. Lines and arrows follow the convention in (a). (d) Residual volume transport in $\theta - S$ space (in bins of 0.01°C [θ] and 0.0025 [S]). The residual-transport-weighted-mean $\theta - S$ coordinates of the inflows and outflows are indicated by solid and dashed symbols, respectively. The coordinates associated with the total flow are marked by squares, and those associated with individual overturning cells are marked by circles. As in Figure 1b-c, isopycnals separating major water masses are indicated by black contours, and those marking the transport maxima of and the boundary between the gyre's two overturning cells are shown by (dashed) grey contours. The freezing point of seawater is shown by the black dashed line. (e) Residual volume transport in $\theta - f_{SIM}$ space (in bins of 0.01°C [θ] and 0.025% [f_{SIM}]). The area

corresponding to the lower cell is indicated by hatching. (f) Residual volume transport in $\theta -$ f_{MET} space (in bins of 0.01°C [θ] and 0.025% [f_{MET}]). The area corresponding to the lower cell is indicated by hatching. (g) Residual volume transports as a function of θ class. Lines and arrows follow the convention in (a).
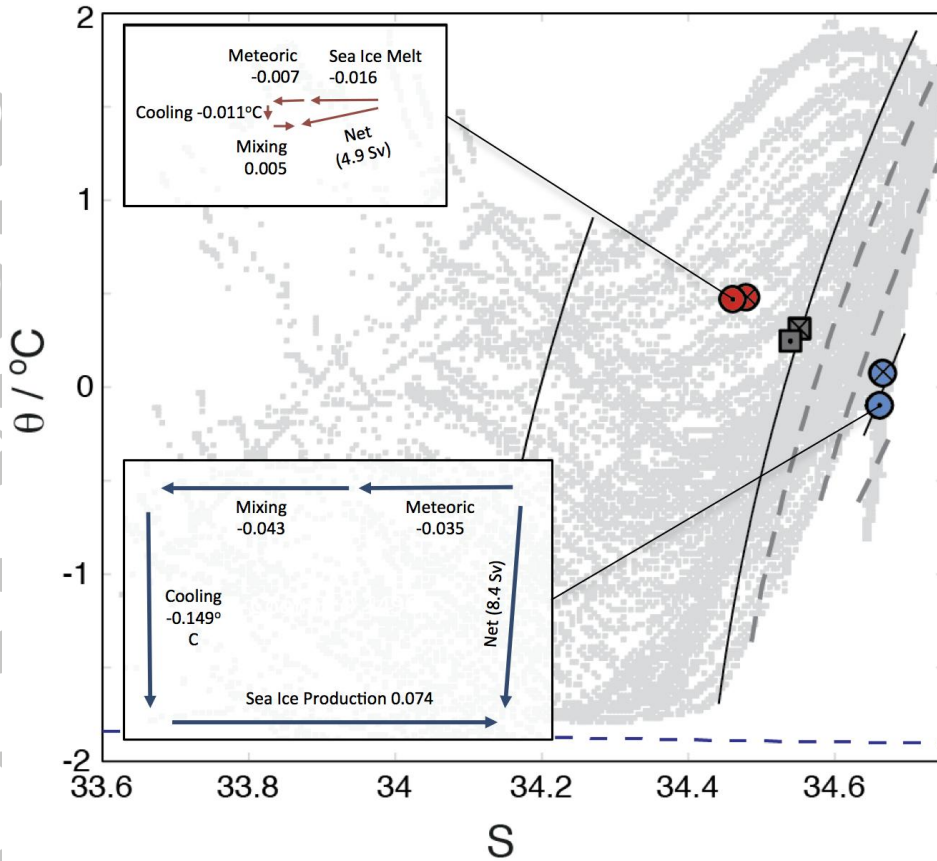
Figure 3. Schematic synthesis of the thermodynamic balance of the Weddell Gyre. The grey shading indicates the area of $\theta - S$ space occupied by water masses along the rim of the gyre. The residual-transport-weighted-mean $\theta - S$ coordinates of the inflows and outflows are indicated by the crossed and dotted symbols, respectively (total flow in grey, upper overturning cell in red, lower overturning cell in blue). As in Figure 1b-c, isopycnals separating major water masses are indicated by black contours, and those marking the transport maxima of and the boundary between the gyre's two overturning cells are shown by (dashed) grey contours. The freezing point of seawater is shown by the black dashed line. The insets show the changes in θ and S associated with individual thermodynamic drivers for each of the overturning cells, where the term 'mixing' refers to exchanges of WW and CDW between the two cells. Arrow lengths are approximately scaled by the represented change in θ or S, and arrow widths by the volume transport of the pertinent overturning cell (denoted in brackets next to the net $\theta - S$ transformation).